

COMPUTATIONAL PROCEDURES FOR POSTBUCKLING OF COMPOSITE SHELLS

G. M. Stanley and C. A. Felippa
Lockheed Palo Alto Research Laboratory
Palo Alto, California

SUMMARY

A recently developed finite-element capability for general nonlinear shell analysis, featuring the use of three-dimensional constitutive equations within an efficient resultant-oriented framework, is employed to simulate the postbuckling response of an axially compressed composite cylindrical panel with a circular cutout. The problem is a generic example of modern composite aircraft components for which postbuckling strength (i.e., fail-safety) is desired in the presence of local discontinuities such as holes and cracked stiffeners. While the computational software does a reasonable job of predicting both the buckling load and the qualitative aspects of postbuckling (compared both with experiment and another code) there are some discrepancies due to (1) uncertainties in the nominal layer material properties, (2) structural sensitivity to initial imperfections, and (3) the neglect of dynamic and local material delamination effects in the numerical model. Corresponding refinements are suggested for the realistic continuation of this type of analysis.

§1. INTRODUCTION

Advanced composite materials, due to their superior strength-to-weight ratios and stiffness tailorability, have become key ingredients in the design of modern aerospace vehicles. However, the complex structural response associated with such materials coupled with the intricacy of their fabrication creates harsh requirements for numerical simulation.

Specifically, a problem that is of current interest to NASA/LaRC is the determination of the postbuckling strength of thin laminated composite shells comprising the "skin" of stiffened air-transport fuselages [1]. These shells are required to maintain safe load-carrying capability substantially beyond the point at which skin buckling (i.e., *wrinkling*) occurs. To complicate matters, aircraft fuselages typically feature local discontinuities, such as fasteners, stiffeners and *cutouts*, which can induce high local stress gradients that tend to *delaminate* the composite material. In the presence of buckling, these local delaminations can propagate throughout — and hence fail — a composite structure.

It is NASA's ultimate goal to be able to predict such phenomena analytically. To this end, they have asked us to match some experimental data obtained for a

representative test specimen [1].* We have completed the first phase of the *global* analysis, which is described in the following sections. It employs a recently developed finite-element shell analysis capability, featuring the use of three-dimensional constitutive equations within an efficient resultant-oriented framework, to determine the buckling load and explore the postbuckling regime of an elastically intact composite model. The more ambitious *global/local* analysis, which involves the prediction of local material delamination and its interaction with global structural response to determine *postbuckling strength*, is still in the planning phase.

§2. PROBLEM DESCRIPTION

§2.1 Setup

The focal problem mentioned above is depicted in Figure 1. Shown is a moderately deep (55.6 deg) cylindrical panel with a circular cutout. The panel has a 14 in. square planform, a 15 in. radius of curvature and a radius-to-thickness ratio of 150. The hole is centrally located and measures 2 in. in diameter. The composite shell wall consists of 16 layers of unidirectional graphite fibers in epoxy-resin. Each layer is .0056 in. thick (for a total of .086 in.) and the layers are arranged in the symmetric, *quasi-isotropic*** stacking sequence: $\{\pm 45/90/0/0/90/\mp 45\}$ degrees — repeated twice. The orthotropic-elastic material properties for each layer are listed in the figure. Note that these properties represent *nominal* values and will require some adjustment in the sequel (see §5).

Surrounded by a metallic test frame, the appropriate boundary conditions for the cylindrical panel are (i) fully clamped on the bottom edge, (ii) clamped except for axial motion on the top edge and (iii) simply supported on the vertical edges.

§2.2 Experimental Results

The test conducted by NASA consisted of statically imposing a uniform end-shortening, δ , to determine the load-carrying capability of the panel beyond the initial buckling load. Experimental results are shown in Figure 2.

Figure 2a represents a normalized “load versus end-shortening” curve. Note that buckling occurs abruptly, followed by a rapid drop in the axial load. Somewhere

* This problem was first suggested by Dr. Norman F. Knight, Jr. at NASA Langley Research Center. We amusingly refer to it as “Knight’s problem” both as an acknowledgment to the originator and as a reminder of the many pitfalls obstructing its numerical solution.

** The term *quasi-isotropic* refers to the fact that the resultant constitutive matrix is essentially isotropic, due to a balanced sequence of fiber angles through the thickness. However, in contrast to truly isotropic materials, there is some additional coupling between bending and twisting deformations.

between the top and bottom of this vertical branch, which spans a period of *milliseconds* in the experiment, delamination occurs near the hole (Fig. 2b). Although the delamination gets progressively worse and eventually distorts the hole, there is a secondary (postbuckling) stiffening branch in the load/displacement curve. The test was stopped at the point on this secondary branch labeled “collapse”, at which point extensive delamination is evident (see [1] for details).

§3. COMPUTATIONAL APPROACH

§3.1 Formulation

The formulation of the governing equations and associated solution algorithms used to analyze the above problem is outlined in Figure 3. A detailed description of this approach may be found in [2]. Briefly, it employs *continuum-based* (CB) shell elements, similar to the Ahmad element [3], but extended to the nonlinear regime and reduced to an economical *resultant* form in which element stiffness and force operators are *pre-integrated* through the thickness.

Shell Equations

Thickness pre-integration of the CB shell equations is achieved by augmenting the standard, Mindlin-type [4] hypotheses of *straight normals* and *zero normal stress* with two additional hypotheses, namely: *small transverse-shear strains* and *mild taper*. As argued in [2], these additional hypotheses do not significantly alter the range of applicability of the original formulation. The resulting theory, which is expressed in terms of stress-resultants rather than pointwise (continuum) stresses, is referred to as a *continuum-based resultant* (CBR) shell formulation.

Note that unlike earlier efforts to pre-integrate the CB shell equations, which typically assume a constant through-thickness variation of the surface metric (*e.g.*, [5]), the present CBR formulation bypasses this assumption and hence is not restricted to very thin shells.

Shell Elements

To spatially discretize the CBR shell equations, a variety of shell finite elements have been implemented within the above framework. However, on the basis of the numerical evaluation conducted in [2], only the following two shell elements were considered for the present analysis: (i) the nine-node Heterosis (HET) element [6], and (ii) a new nine-node assumed natural strain (ANS) shell-element [7]. While both elements are parabolically curved (Fig. 3) and use standard isoparametric interpolation as a starting point, each departs from the basic recipe in order to properly represent inextensional bending deformation for thin shells.

In particular, the 9_HET element *selectively under-integrates* all stiffness and force terms involving membrane strains to avoid membrane “locking”, and uses a mixture of Lagrange shape functions (for rotations) and Serendipity shape functions (for translations) to avoid “spurious modes” otherwise evoked by reduced integration.

In contrast, the 9_ANS element assumes an appropriate (inextensionally accurate) strain field from the outset, using a modified set of Lagrange shape functions and employing full numerical integration throughout. Due to the fact that the strains are assumed in the generally *non-orthogonal* isoparametric coordinate basis, an apparent advantage of the ANS approach is its decreased sensitivity to element mesh distortion.

Nonlinear Solution Procedures

After performing an *updated-Lagrange* linearization of the equilibrium equations, a modified Newton-Raphson (NR) version of the Riks-Crisfield (RC) arc-length control algorithm [8] is used to trace incrementally the load-displacement curve. The RC procedure was adopted as a convenient means of statically traversing the bifurcation points that arise in shell postbuckling analysis. However, such methods are not foolproof, and special attention by the analyst (*e.g.*, in the selection of imperfections, step-sizes and error tolerances) is often required in the vicinity of closely spaced or *multiple* bifurcation points.

Two kinds of update procedure are required to advance the solution of the discrete nonlinear shell equations from one load-step to the next: (i) a *kinematic* update that “accumulates” incremental *nodal displacement* — both translational and rotational components; and (ii) a *constitutive* update that generates new *element stresses* from the corresponding displacement field.

Only the *rotational* part of the kinematic update is non-trivial.* In the present approach, the rotation increments are used to update *orthogonal triads* defined at each shell node. The triad-update algorithm involves no trigonometric functions, maintains orthogonality at each step and provides a shell-oriented coordinate system in which the *normal rotational* degree of freedom may be eliminated at all shell nodes (except at junctures). Furthermore, once the nodal triads and reference-surface coordinates have been so updated, the *current* element configuration is completely and uniquely defined (see [2] and [9] for details).

The *stress update* is handled via an incrementally objective algorithm [10] that

* Since the translational components of displacement are *vectorial*, translation increments are simply *added* to obtain total displacements and hence update the nodal coordinates.

features a midpoint-rule numerical integration of rate-type constitutive equations. For finite-strain analysis, the constitutive algorithm additionally involves shell *thickness updates* that account for large Poisson effects. These are computed (as in [11]) by recovering the normal strain increments from the constitutive equations via the zero normal stress (ZNS) hypothesis.

Summary of Computational Features

The computational features of the above approach may be summarized as follows:

- Applicable to Both Thin and Moderately Thick Shells
- Rotations May Be Arbitrarily Large
- Strains May Be Large (Except Transverse Shears)
- Resultant Format Yields $\text{Cost Savings} \propto \text{Number of Layers}$
- Shell Elements Are Fairly Robust
 - No Locking
 - No Spurious Mechanisms
 - Low Sensitivity to Mesh Distortion (Especially ANS Elements)

Finally, note that while the formulation allows for finite strains and inelastic material behavior, the present analysis simply employs *orthotropic linear-elasticity* within each layer and *does not* account for the material delamination (*i.e.*, damage) observed in the NASA experiment.

§3.2 Implementation (NICE Software Architecture)

The shell-element capabilities mentioned above have been implemented in a modular fashion to facilitate research and transferral to other finite element codes. Some of the specific shell-element functions that are available via independent FORTRAN77 subroutine calls are shown in Figure 4a. A complete description of the shell-element software (including listings) is given in Appendix S of reference [2].

The *host finite-element program* used by the authors is actually a *network* of independently executable programs (or *processors*) which are coordinated via high-level *procedures* written in a mathematically oriented command-language (Fig. 4b). In such an environment, the shell-element software is embedded in a single *processor* and the global solution algorithms are implemented as *procedures*; examples are given in [12].

The software architecture (*i.e.*, utilities) used to construct this particular analysis system is known as NICE (for *Network of Interactive Computational Elements*, [12,13]). Due to the flexibility provided by the NICE architecture and its suitability for nonlinear and coupled-field problems, it is currently being explored by NASA as the basis for a standard generic *testbed* system for Computational Structural Mechanics (see [14] and other presentations therein). One of the motivating factors for developing such a system is the implementational complexity associated with a comprehensive global/local analysis of the present composite-shell problem.

§4. FINITE-ELEMENT MODELS

Due to the physics of the problem, a *full* numerical model of the test specimen is required (Fig. 5). The slight anisotropy emanating from the composite material stacking sequence is only partly responsible for the lack of available symmetry.* As will become apparent, the nonlinear postbuckling response is *inherently* non-symmetric due to the presence of the hole and the participation of many diverse mode shapes.

Several combinations of shell-element type and mesh density were employed during the course of the linear (pre-buckling), stability (buckling eigenvalue) and nonlinear (postbuckling) analyses. Figure 5 shows three representative grids, involving 300, 1500 and 5000 degrees-of-freedom, respectively. These grids correspond to 16, 80 and 256 nine-node elements (or alternatively to 64, 320 and 1024 four-node elements), respectively. Note that there is intrinsic element mesh-distortion in these models — both in-plane and out-of-plane — due to the focus on the hole and the curvature of the shell. However, the elements nearest the hole (where it counts most) have the most regular shapes.

The coarsest grid (1) was used to *verify* the modeling procedure, the finest grid (3) was used exclusively to check convergence of the *linear* and *eigen* solutions, and the intermediate grid (2) became the workhorse for *nonlinear* analysis. Furthermore, as little difference was observed between the 9_HET and 9_ANS elements (§3.1) during the early stages of analysis, the 9_HET element (which is slightly less expensive) is featured in the analytical results that follow.

Boundary conditions were imposed as described in Section 2 and illustrated in Figure 5. To simulate end-shortening, an axial *force* was applied in conjunction with a *degree-of-freedom equivalence* among all axial displacements on the loaded edge. This was done to avoid the use of *specified displacements*, which tend to complicate the adaptive, arc-length-based nonlinear solution algorithm.

* We have confirmed this via numerical experiments with an *isotropic* model.

§5. LINEAR (PRE-BUCKLING) ANALYSIS

Results for the linear pre-buckling analysis are shown in Figure 6. The deformations due to an applied axial compressive load of 22480 lbs (1 kN) are shown magnified by a factor of 10 in the top half of the figure — for grid 2. The corresponding distribution of the axial stress resultant, N_x , along the panel circumference at mid-span is shown in the bottom half of the figure — for both grids 2 and 3.

Regarding the *displacement* solution, convergence of the axial end-shortening, δ , was achieved with grid 2. (Grid 3 yielded less than a 1% increase in end-shortening.) However, the converged end-shortening solution, $\delta = .0316$, is approximately 15% lower than the experimental value; as deduced from the linear portion of the experimental load-displacement curve (Fig. 2). It is presumed that this over-estimation of the axial stiffness is due to the uncertainty in the *nominal* material properties, a conclusion that is reinforced in §8. Thus, to compensate for the mismatch, the lamina principle elastic modulus (E_1) is reduced by a corresponding factor in the subsequent nonlinear analysis (§7).

From a qualitative perspective, the solution shows substantial bending deformation in the vicinity of the hole (Fig. 6a). This suggests that geometric nonlinearity may be important even at relatively low load levels and diminishes the credibility of linear response and buckling-eigenvalue analyses.

Regarding the linear *stress* solution, note that the compressive axial resultant, N_x , is distributed evenly along most of the panel circumference except for a very localized region near the hole. While grid 2 was adequate for the *displacement* solution, grid 3 provides much more accurate resolution of this *stress concentration*. In particular, grid 2 yielded a peak stress concentration factor (SCF) of 2.8; about 14% less than the SCF obtained with grid 3.

As experimental data were not available for verification of the computed stresses, the convergence of the grid 3 stress solution was inferred by comparison with a closed-form (asymptotic) solution due to C.R. Steele (private communication, Stanford University, 1985). While the closed-form solution pertained to a purely *isotropic* panel, the linear finite-element stress solutions for isotropic and quasi-isotropic panels were found to be quite similar. It is also interesting that the SCFs for both the *isotropic* model (3.1) and the *quasi-isotropic* model (3.25) are not very different from the classical SCF for a *flat plate* with a circular hole (3.0).

Finally, note that by strongly *biasing* the mesh towards the hole, it was possible to obtain grid-3 accuracy with grid 2 for the local stress gradients. Such biasing, however, was found to be unnecessary in the subsequent, globally oriented buckling and postbuckling analyses.

§6. STABILITY (BUCKLING) ANALYSIS

Figure 7 shows the first 5 buckling eigenmodes for grid 2. These results represent perturbations about the linear pre-buckling solution described. The eigenvalues, $\lambda = 1.084, 1.106, 1.181, 1.432, 1.582$, are the ratios of the corresponding buckling loads to the axial load applied in the linear pre-buckling analysis. As before, grid 2 seems to provide adequate resolution, with grid 3 giving only a 2% reduction in the first two eigenvalues, and a 4% reduction in the remaining three.

The following observations are important for subsequent computational purposes: (i) the eigenvalues are closely spaced; (ii) the eigenmodes are vastly different in character; (iii) there is no *single* form of symmetry to be exploited computationally; (iv) the first buckling mode is symmetric and bears the most resemblance to the linear pre-buckling solution; (iv) the second and third modes possess *skew* symmetries; (v) the fourth and fifth modes are symmetric; the latter mode featuring practically no distortion of the circular hole; and (vi) higher modes (not shown) look much like those for a cylindrical panel *without* a hole, though the values remain closely spaced.

Finally, it was found that the first (*i.e.*, critical) buckling load is approximately 25% lower than that of an identical cylindrical panel without a hole. Hence, while the influence of the hole on the buckling *load* is only moderate (*i.e.*, relative to the stress concentration factor), its influence on the buckling *modes* is profound. As we shall see, the hole has an even stronger influence on the postbuckling response.

§7. NONLINEAR (POSTBUCKLING) ANALYSIS

In practice, more than just a linearly converged model and an adaptive solution strategy were necessary to obtain a reasonable *nonlinear* solution. One additional pre-requisite was a 15% reduction in the nominal elastic modulus, E_1 (from 19.6×10^6 to 17.1×10^6), to match the linear branch of the load versus end-shortening curve (as explained in §5). Another important ingredient was the specification of *initial imperfections*. In this regard, three versions of the analysis were run: (1) one involving no imperfections; (2) one with an imperfection amplitude of 1% of the thickness applied to each of the first 4 buckling modes (see Fig. 7); and (3) one with an imperfection amplitude of 10% of the thickness applied to each of the first 4 buckling modes. A discussion of the results for these three cases follows.

§7.1 No Imperfections

One would think that the out-of-plane “imperfections” introduced by the linear pre-buckling solution (Fig. 6) would be sufficient to trigger a realistic buckling response. However, this was not the case. With no imperfections, the computed solution path resembled the experiment only up to the descending part of the

load-displacement curve (Fig. 8a). The computed curve then rolled back onto itself with the stiffening branch of the postbuckling curve practically aligned with the *pre-buckling* curve.

To gain further insight, it is useful to look at the deformation and stress histories portrayed in Figure 8b. Shown is a sequence of computational “snapshots” taken at various points (*i.e.*, load steps) on the nonlinear load-displacement curve.* The variation of the axial stress resultant along the mid-span circumference is plotted below each frame.

Note that the deformation starts out (at load step 10) much like the first linear buckling mode (Fig. 7), with inward dimples both fore and aft of the hole, then *articulates* through the second and third modes during the initial postbuckling phase (steps 15–20). This *rotation* of the two dimples about the hole is probably triggered by the bending/twisting coupling inherent in the composite stacking sequence. The dimples continue to rotate and broaden until, at step 40, the pattern begins to resemble the *fifth* linear buckling mode. Evidently, it is this “locking” into mode 5 that is responsible for the excessive secondary stiffening in the load-displacement curve (Fig. 8a). Clearly, mode 5 is an unrealistically *stiff* one, resembling what might occur if a ring *stiffener* had been placed around the hole. This is also evident in the axial stress distribution, where the stress concentration has practically been *shed* by step 40.

§7.2 Large Imperfections

To avoid the unrealistic mode-5 locking observed in the preceding analysis, a fairly large initial imperfection was introduced in the numerical model. This was accomplished by adding an equal measure of each of the first 4 buckling modes to the initial geometry, such that the maximum radial (*i.e.*, shell-normal) displacement in each mode was equal to 10% of the panel thickness. Thus, the magnitude of the combined radial imperfection approached 40% of the thickness at some points. It is emphasized that this rather arbitrary choice of imperfections was designed primarily to minimize the influence of mode 5.

The computed nonlinear response for the imperfect panel is shown in Figure 9. Note that the secondary stiffening branch bears more resemblance to the experiment than did the imperfection-less analysis. Unfortunately, it is also true that the buckling (*i.e.*, peak) load has dropped by about 15%, and now underestimates the *experimental* buckling load by more than 20%. A heuristic explanation is

* Note that the pre-buckling phase of the analysis appears *linear* with respect to the axial displacement, δ . However, due to the rapid growth in *radial* displacements (not shown), the analysis is actually quite nonlinear from the outset; which explains the relatively large number of load-steps required on the “linear” branch of Fig. 8.

provided by considering the deformation and stress histories.

In Figure 9b, we see that with the 10%-h imperfections, the buckling pattern leaves mode 1 almost immediately and develops an intensified inward dimple on one side of the panel. Consequently, the full axial load is re-distributed to the *other* side of the panel (see N_x plots in Fig. 9b), accounting for the reduction in both the buckling load and the postbuckling stiffness (fig. 9a).

§7.3 Small Imperfections (the "Bottom Line")

Finally, the "best of both worlds" was obtained with a 1%-h imperfection in each of the first 4 modes. Compared with the previous analysis, the computed load-displacement curve (Fig. 10) shows both an increase in the maximum load and a decrease in the minimum load, thus bringing the solution more in line with experiment.

The improved performance, obtained by reducing the imperfections, may again be related to the deformation history (Fig. 10b). Here, as in the case without imperfections, two inward dimples develop and proceed to rotate about the hole. Just after buckling, however, one dimple tends to deepen while the other diminishes, and eventually there is a *double* snap-through. This accounts for the double dip in the load-displacement curve (Fig. 10a) and seems to explain why a lower minimum load is obtained with the smaller imperfection.

Still, there are some serious discrepancies between analysis and experiment, namely: (i) a 7% under-estimation of the buckling load, (ii) a 25% over-estimation of the minimum load, (iii) a 30% under-estimation of the postbuckling end-shortening, and (iv) a 10% over-estimation in the postbuckling stiffness. These will be addressed in §9.

§8. CORROBORATION WITH ANOTHER CODE

To support the above results, obtained via the computational procedures described in Section 3, parallel analyses were performed with another finite-element computer code. For this purpose, we employed the STAGS code [15], which has been used for more than a decade by various government agencies and industrial firms (*e.g.*, NASA and Lockheed) to analyze difficult nonlinear shell problems. Another reason for using STAGS is that it features finite-element computational procedures that are substantially different from those used in the present approach, thus adding strength to an analytical comparison.

For the *linear* (pre-buckling and buckling) analysis, excellent agreement was obtained between the STAGS and NICE-based solutions. For completeness, the STAGS runs were performed with two radically different shell-element types, which both converged to the same solution as the NICE/9.HET element, albeit at slower

rates and from *below* in stiffness. (Note that while the axial pre-buckling stiffness of the STAGS elements converged from below, the *buckling loads* converged from *above*).

In particular, the comparison included: (i) the commonly used STAGS/410 element — a flat quadrilateral plate element based on Kirchhoff-Love theory and cubic membrane/bending displacement interpolation; and (ii) the less frequently used STAGS/422 element — a quadrilateral composed of two Kirchhoff-based triangular plate sub-elements with cubic bending interpolation and quadratic membrane interpolation. It is believed that the relatively slow convergence “from below” of the STAGS/410 element is due to *warping sensitivity*, while that of the STAGS/422 element is probably due to the *incompatibility* between membrane and bending displacement fields for non-flat quadrilateral element shapes.*

For the *nonlinear* comparisons with NICE/9.HET, the STAGS/410 element was used exclusively. The resulting load-displacement curves (for 1%-h and 10%-h imperfections) are summarized in Figure 11. The dashed curves represent the NICE/9.HET solutions and the dotted curves represent the STAGS/410 solutions; both were obtained with Grid 2 (Fig. 5).

Note that although the STAGS and NICE-based solutions use different finite-element types, large-rotation update procedures and nonlinear solution strategies, the correlation is remarkable — especially during the postbuckling phase. Even the STAGS zero-imperfection analysis (not shown) resulted in the same excessive postbuckling stiffness as displayed in Figure 8a. One other point: While the STAGS/410 element consistently shows about a 5% higher buckling load than the NICE/9.HET element, thus coming closer to the experimental peak; STAGS/410 is actually *less* accurate — with respect to *discretization* errors — than NICE/9.HET. This follows from the fact that both STAGS/410 and NICE/9.HET converge from *above* in the buckling load. This was confirmed by running the NICE/9.HET element with a *coarser grid*, for which it too showed a 5% higher peak. That non-converged solutions compare better with experiment than converged ones suggests that spatial discretization is not the only source of error here (e.g., see §9).

* It is interesting to note that the STAGS/422 element was used in the related study conducted in [1], where it yielded a 17% more flexible linear solution, and thus agreed better with the linear portion of the experiment. Nevertheless, it has since been found that the boundary conditions were not consistently applied to the element's *mid-side* freedoms in that analysis. By correcting this implementation error, the 17% discrepancy with the other elements has been completely eliminated. Thus, it appears that the “accuracy” obtained in [1] with the STAGS/422 element is due to compensating errors in the nominal material properties.

§9. CONCLUSIONS

§9.1 Summary

The present study may be summarized as follows:

- PURPOSE:
 - Validate continuum-based resultant (CBR) shell formulation
 - Evaluate new shell elements
 - Gain experience with composite-shell postbuckling analysis
- RESULTS:
 - Good agreement in pre-buckling/buckling range
 - Good *qualitative* agreement in postbuckling range
 - Discrepancies due to:
 - *Material properties*
 - *Imperfection sensitivity*
 - *Dynamic effects*
 - *Delamination*

The “good” agreement obtained between the present shell-element formulation and experiment in the pre-buckling and buckling range was possible only after adjusting the nominal material properties so that the linear axial stiffnesses coalesced. The material-property modification was further justified via corroboration with the STAGS finite-element code, which features a substantially different computational approach.

The “best” solution for the nonlinear response was obtained by introducing small (1%-thickness) imperfections corresponding to each of the first four buckling modes. The computed load-displacement curve (Fig. 10a), which again compared well with STAGS (Fig. 11), still showed major discrepancies with the experiment: The discrepancy in the *buckling load* (which is relatively small) may be due to the inadequacy of adjusting only the principal layer elastic modulus, E_1 , rather than the complete set of orthotropic material constants. The discrepancy in the *unloading* phase of postbuckling (*i.e.*, the computed end-shortening *reversal*) is attributed to the quasi-static approximation of what is, in reality, a *dynamic* phenomenon. Finally, the discrepancy in the *stiffening* phase of postbuckling is clearly dominated by damage, *i.e.*, delamination observed in the experiment but not represented in the model.

§9.2 Recommendations

The goal is to eliminate the discrepancies listed with a minimum of computational cost and complexity. To this end, the following steps are recommended:

1) *PERFORM ADDITIONAL EXPERIMENTS*. First, more experimental data are required to verify existing computational capabilities for composite shell post-buckling. For example, panel imperfections should be carefully measured and selected strains and overall deformation patterns should be monitored at frequent intervals. Additionally, an isotropic panel should be tested in order to eliminate the material identification problem and also to provide a standard *benchmark for shell-element evaluation*. The isotropic problem would be valuable for screening out geometrically sensitive elements.

2) *REFINE NONLINEAR GRID*. The nonlinear analysis should be repeated with a finer grid (*e.g.*, Grid 3), as convergence in the linear regime is no guarantee of convergence in the nonlinear regime. Moreover, a study of modal participation both in the imperfections and in the nonlinear response may help establish modeling guidelines for future analysis.

3) *INCLUDE DYNAMIC EFFECTS*. Dynamic effects, which are relatively straightforward to incorporate, should be assessed at the first opportunity. The analysis could be started in a quasi-static mode, switched to an *explicit* transient response algorithm during the unstable phase, and switched again to an *implicit* algorithm during the stable postbuckling phase.

4) *REPRESENT LOCAL FAILURE (DELAMINATION)*. To account for the composite delamination mechanism, appropriate *failure criteria* and *progressive-failure modeling procedures* need to be developed, implemented and evaluated. For shell-based failure criteria, *accurate stress recovery* is essential. Improved stress resolution is required both *along the surface* (*e.g.*, via stress/displacement iterations and adaptive refinement) and *through-the-thickness*, as both normal and transverse-shear stresses can play a dominant role in delamination. Progressive failure may then be simulated by methods ranging from a simplified shell model that *selectively degrades layer properties*, to a full *3D analysis near the hole* with an evolving 2D/3D transition. An intermediate approach is to “split” shell elements along delaminating boundaries. (See Fig. 12.) The simplest approach, however, has obvious implementational advantages.

5) *DEVELOP EFFICIENT GLOBAL/LOCAL ALGORITHMS*. Finally, there is a need to reduce the cost of nonlinear analysis for such problems. The cost of the *global* analysis is dominated by the large number of iterations/steps in the linear-to-postbuckling transition regime. Possible approaches include the reduced-basis

technique [16,17], Thurston's method [18], and improved extrapolators. For the combined *global/local* problem, where material "properties" are changing rapidly during postbuckling, additional features such as line-searches [19], quasi-Newton stiffness updates [20] and nonlinear substructuring may greatly improve efficiency.

We are presently acting on recommendations (2)–(3) and will report the outcome in a forthcoming paper.

ACKNOWLEDGMENTS

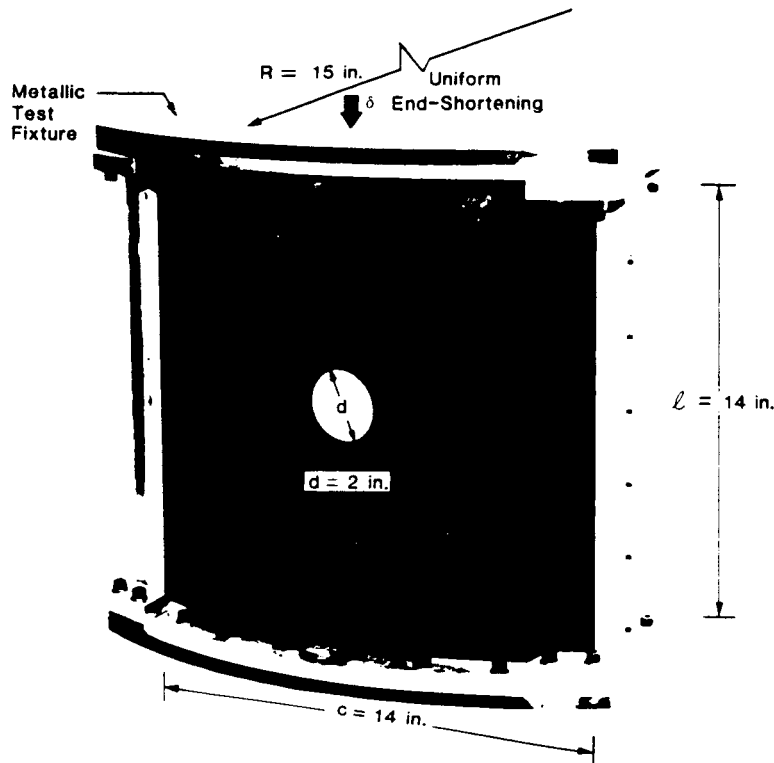
The preparation of this paper was supported by the Independent Research Program of Lockheed Missiles and Space Company, Inc. Ongoing research is being supported by NASA/Langley Research Center as part of their newly launched program in Computational Structural Mechanics.

REFERENCES

- [1] Knight, N.F., Jr. and Starnes, J.H., Jr. (1984), "Postbuckling Behavior of Axially Compressed Graphite-Epoxy Cylindrical Panels with Circular Holes", presented at the 1984 ASME Joint Pressure Vessels and Piping / Applied Mechanics Conference, San Antonio, Texas.
- [2] Stanley, G.M. (1985), *Continuum-Based Shell Elements*, Stanford University Ph.D. thesis, also Lockheed report LMSC-F035839.
- [3] Ahmad, S., Irons, B.M. and Zienkiewicz, O.C. (1970), "Analysis of Thick and Thin Shell Structures by Curved Finite Elements", *International Journal for Numerical Methods in Engineering*, **2**, 419–451.
- [4] Mindlin, R.D. (1951), "Influence of Rotatory Inertia and Shear on Flexural Motions of Isotropic, Elastic Plates", *Journal of Applied Mechanics*, **18**, 31–38.
- [5] Parisch, H. (1981), "Nonlinear Analysis of Shells Using Isoparametric Elements", pp. 47–63 in *Nonlinear Finite Element Analysis of Plates and Shells*, (eds. T.J.R. Hughes et al.), ASME, New York.
- [6] Hughes, T.J.R., and Cohen, M. (1979), "The 'Heterosis' Finite Element for Plate Bending", *Computers and Structures*, **9**, 445–450.
- [7] Park, K.C. and Stanley, G.M. (1986), "A Curved C^0 Shell Element based on Assumed Natural-Coordinate Strains", in *Journal of Applied Mechanics*, June 1986.
- [8] Crisfield, M.A. (1983), "A Fast Incremental/Iterative Solution Procedure that Handles Snap-Through", *Computers and Structures*, **13**, 55–62.
- [9] Rankin, C.C. and Brogan, F.A. (1984), "An Element-Independent Corotational Procedure for the Treatment of Large Rotations", pp. 85–100 in *Collapse Analysis of Structures* (eds. L.H. Sobel and K. Thomas), ASME, New York.

- [10] Hughes, T.J.R. and Winget, J. (1980), "Finite Rotation Effects in Numerical Integration of Rate Constitutive Equations Arising in Large-Deformation Analysis", *International Journal for Numerical Methods in Engineering*, **15**, 1862–1867.
- [11] Hughes, T.J.R. and Carnoy, E. (1981), "Nonlinear Finite Element Shell Formulation Accounting for Large Membrane Strains", pp. 193–208 in *Nonlinear Finite Element Analysis of Plates and Shells* (eds. T.J.R. Hughes et al.), ASME, New York.
- [12] Felippa, C.A. and Stanley, G.M. (1985), "NICE: A Utility Architecture for Computational Mechanics", proceedings of US-Europe Symposium on Finite-Element Methods for Nonlinear Problems, Univ. of Trondheim, Norway (ed. by P. Bergan).
- [13] Felippa, C.A. (1981), "Architecture of a Distributed Analysis Network for Computational Mechanics", *Computers and Structures*, **13**, 405–413.
- [14] Geers, T.L. (1984), "Comments on Proposed Research Program in Computational Structural Mechanics", proceedings of *Workshop on Computational Structural Mechanics*, held 5–7 Sep 1984 at NASA/LaRC, edited by W.J. Stroud.
- [15] Almroth, B.O., Brogan, F.A. and Stanley, G.M. (1979), "Structural Analysis of General Shells, Vol. II: User Instructions for the STAGS(C-1) Computer Code", Lockheed Report LMSC-D33873.
- [16] Noor, A.K. and Peters, J.M. (1983), "Recent Advances in Reduction Methods for Instability Analysis of Structures", *Computers and Structures*, **16**, 67–80.
- [17] Stehlin, P. and Brogan, F.A. (1984), "Analysis of Structural Collapse by the Reduced Basis Technique", pp. 69–84 in *Collapse Analysis of Structures* (eds. L.H. Sobel and K. Thomas), ASME, New York.
- [18] Thurston, G.A., Brogan, F.A. and Stehlin, P. (1985), "Postbuckling Analysis Using a General Purpose Code", presented at AIAA 26th Structures, Structural Dynamics and Materials Conference, Orlando, Florida, AIAA Paper No. 85-0719-CP.
- [19] Crisfield, M.A. (1982), "An Arc-Length Method Including Line Searches and Acceleration", *International Journal for Numerical Methods in Engineering*, **19**, 1269–1289.
- [20] Dennis, J.E. and Moré, J.J. (1977), "Quasi-Newton Methods, Motivation and Theory", *SIAM Review*, **19**, 46–89.

COMPOSITE CYLINDRICAL PANEL WITH CIRCULAR HOLE



NOMINAL COMPOSITE MATERIAL PROPERTIES:

16 Layers
 Graphite-Epoxy
 $h_{\text{layer}} = 0.0056$ in.
 $h_{\text{total}} = 0.09$ in.
 $E_1 = 19.6 \times 10^6$ psi
 $E_2 = 1.89 \times 10^6$ psi
 $\nu_{21} = 0.38, \nu_{12} = 0.037$
 $G_{12} = 0.93 \times 10^6$ psi
 $\{\pm 45/90/0/0/90 \mp 45\}^\circ \text{ sym}$

Figure 1. Knight's problem, NASA test specimen.

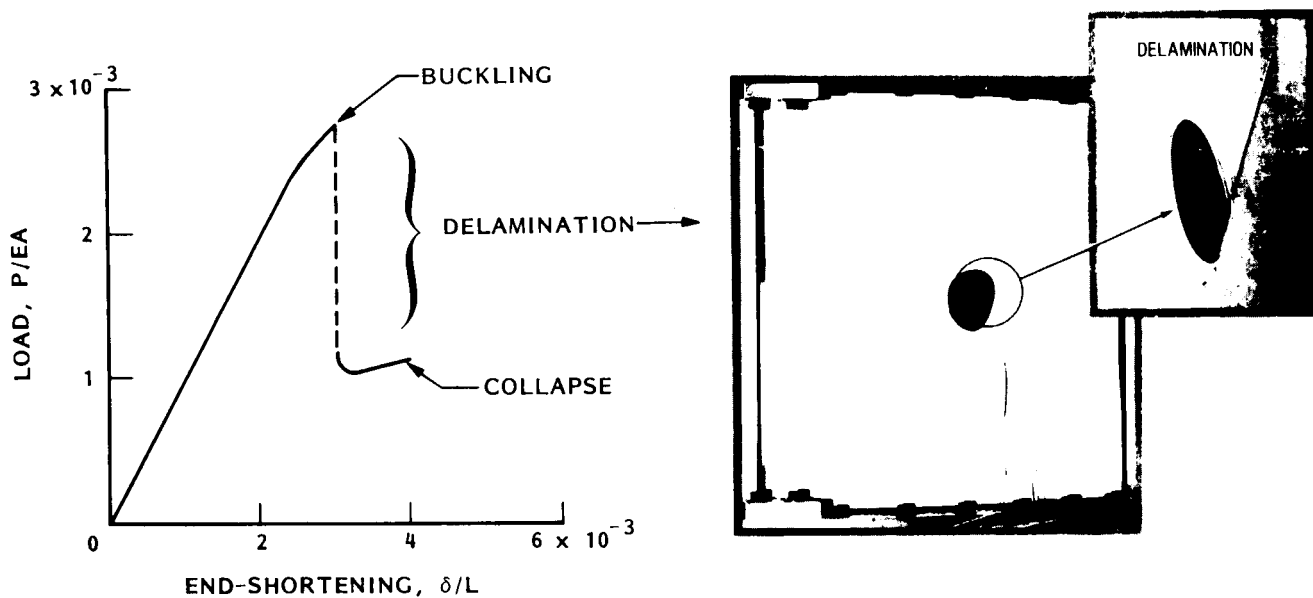


Figure 2. Experimental results.

ORIGINAL PAGE
 BLACK AND WHITE PHOTOGRAPH




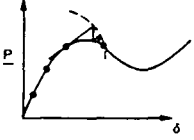

<ul style="list-style-type: none"> Continuum-based (CB) shell equations <ul style="list-style-type: none"> 3-D Continuum equations (equilibrium/constitutive) Embed shell hypotheses (straight normals, zero normal stress) 	
<ul style="list-style-type: none"> Reduce to "resultant" (CBR) form <ul style="list-style-type: none"> Assume: small transverse-shear strains, mild taper Preintegrate through-the thickness 	
<ul style="list-style-type: none"> Discretize via curved "isoparametric" elements <ul style="list-style-type: none"> Selective/reduced integration (SRI) Assumed natural strain (ANS) 	
<ul style="list-style-type: none"> Solve nonlinear matrix equations via: <ul style="list-style-type: none"> Linearization w.r.t. current configuration (UL) Modified NR algorithm with adaptive (RC) strategy Nodal triad updates for large rotations 	
<ul style="list-style-type: none"> Solve rate constitutive equations via: <ul style="list-style-type: none"> "Midpoint rule" incremental algorithm ZNS recovery of normal strains (thickness updates) 	

Figure 3. Computational approach.

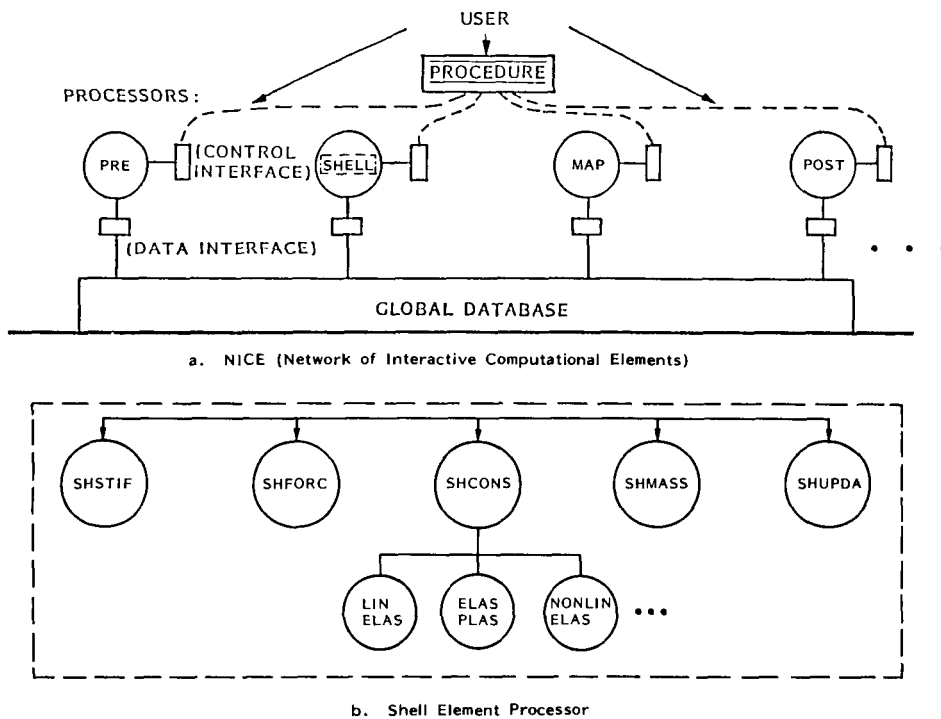


Figure 4. Implementation.

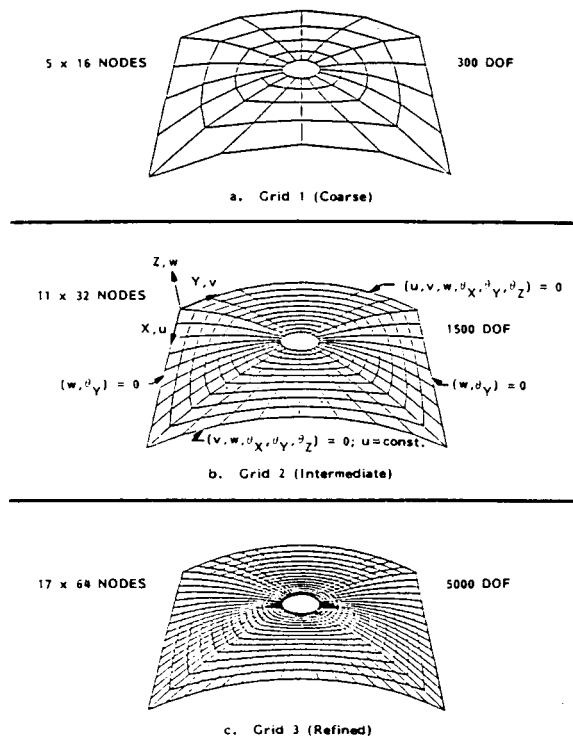


Figure 5. Finite-element models.

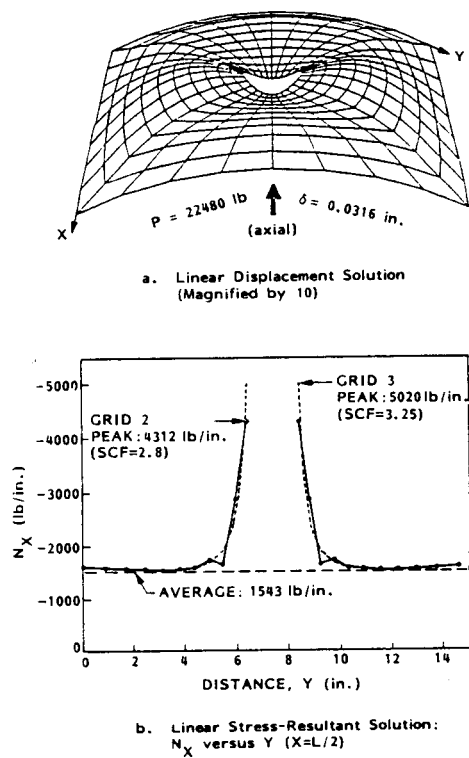


Figure 6. Linear (prebuckling) analysis.

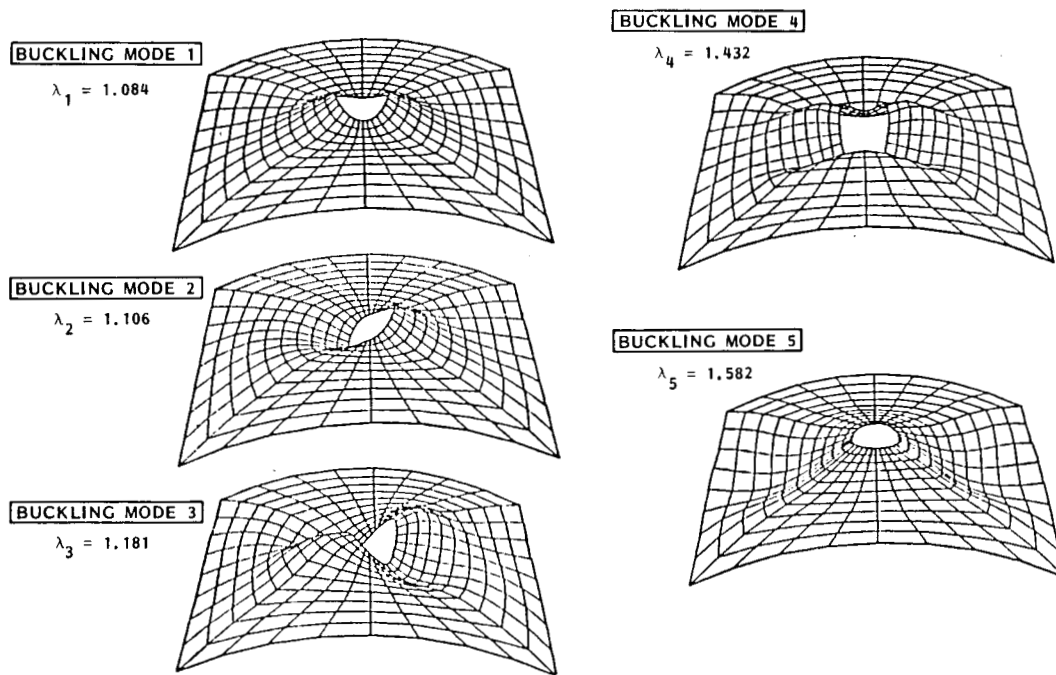


Figure 7. Stability (buckling eigenvalue) analysis.

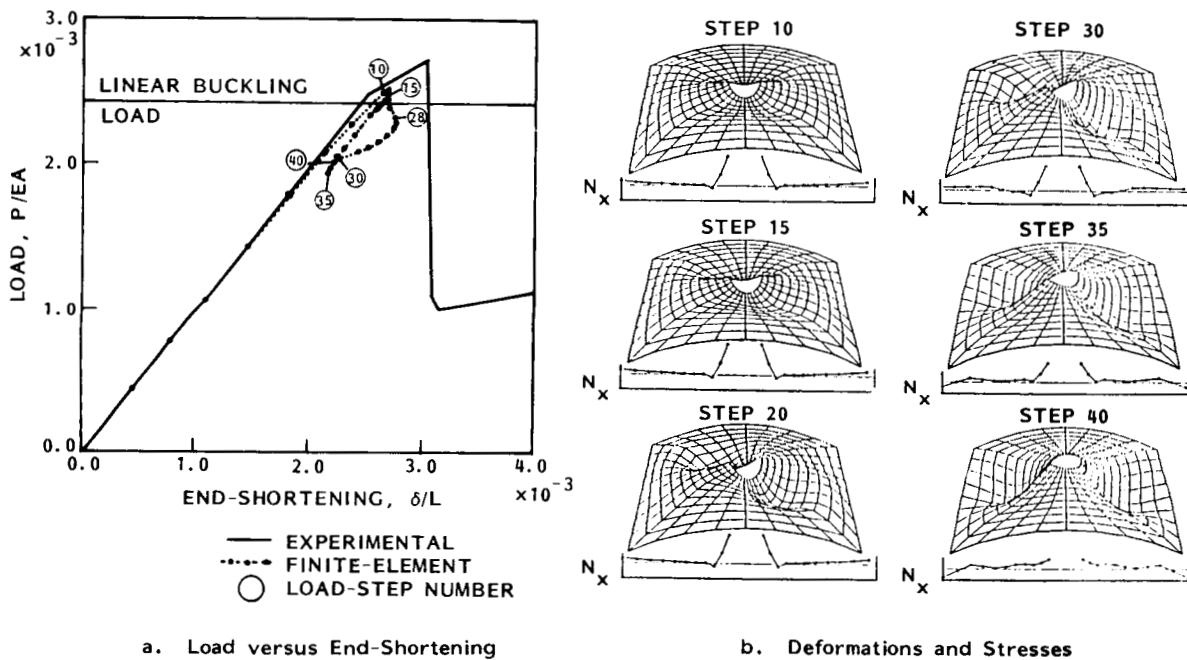


Figure 8. Nonlinear (postbuckling) analysis; no imperfections.

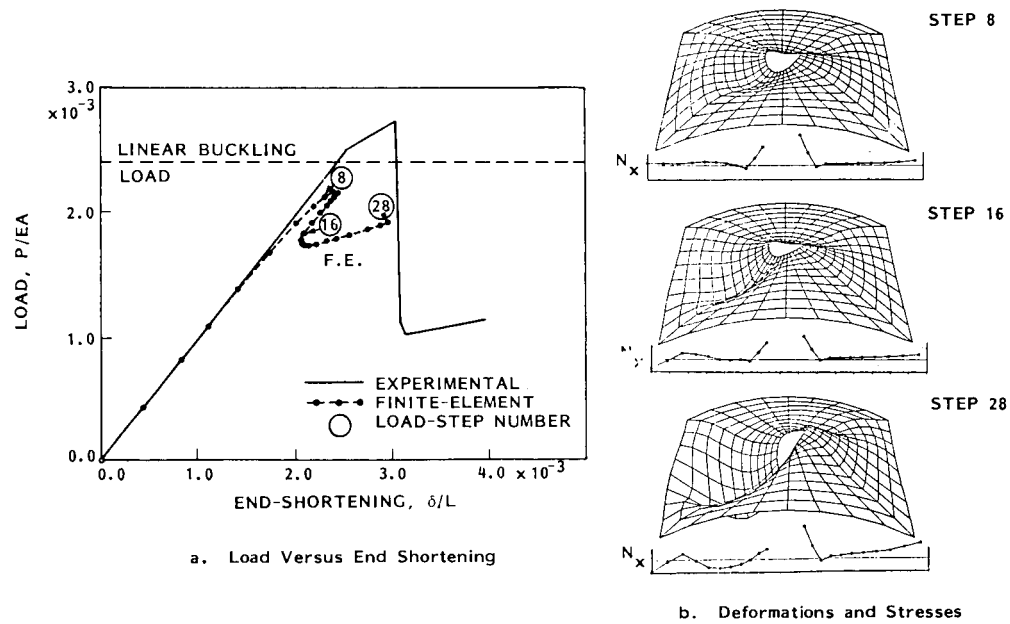


Figure 9. Nonlinear (postbuckling) analysis; 10%-h imperfections.

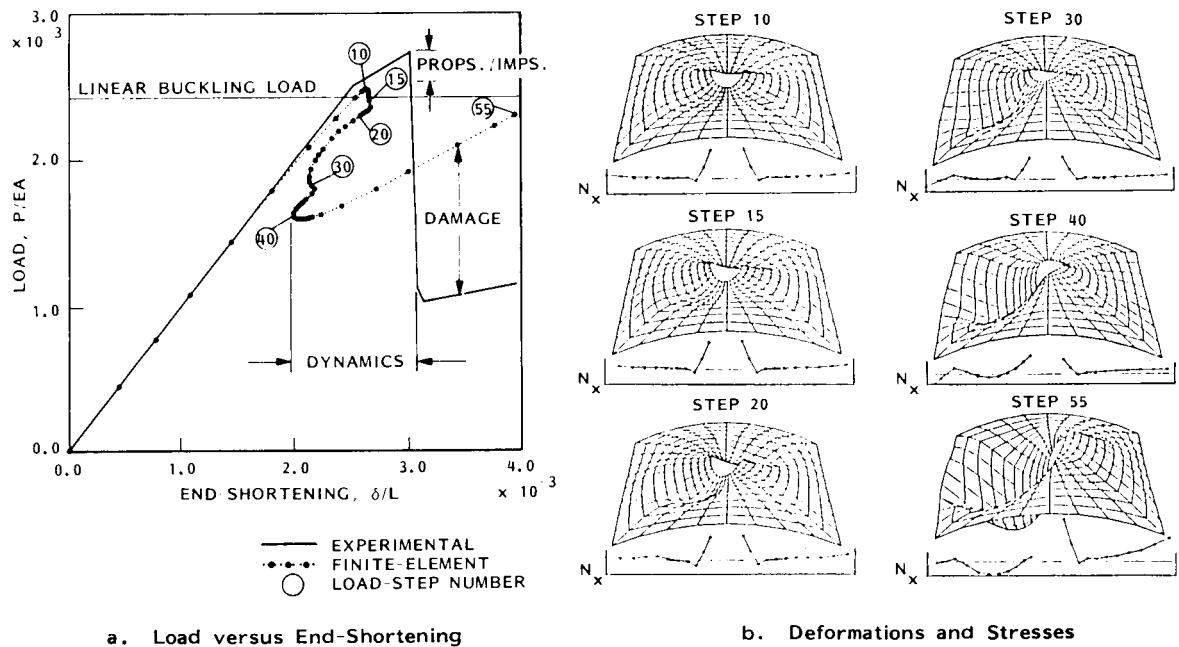


Figure 10. Nonlinear (postbuckling) analysis; 1%-h imperfections.

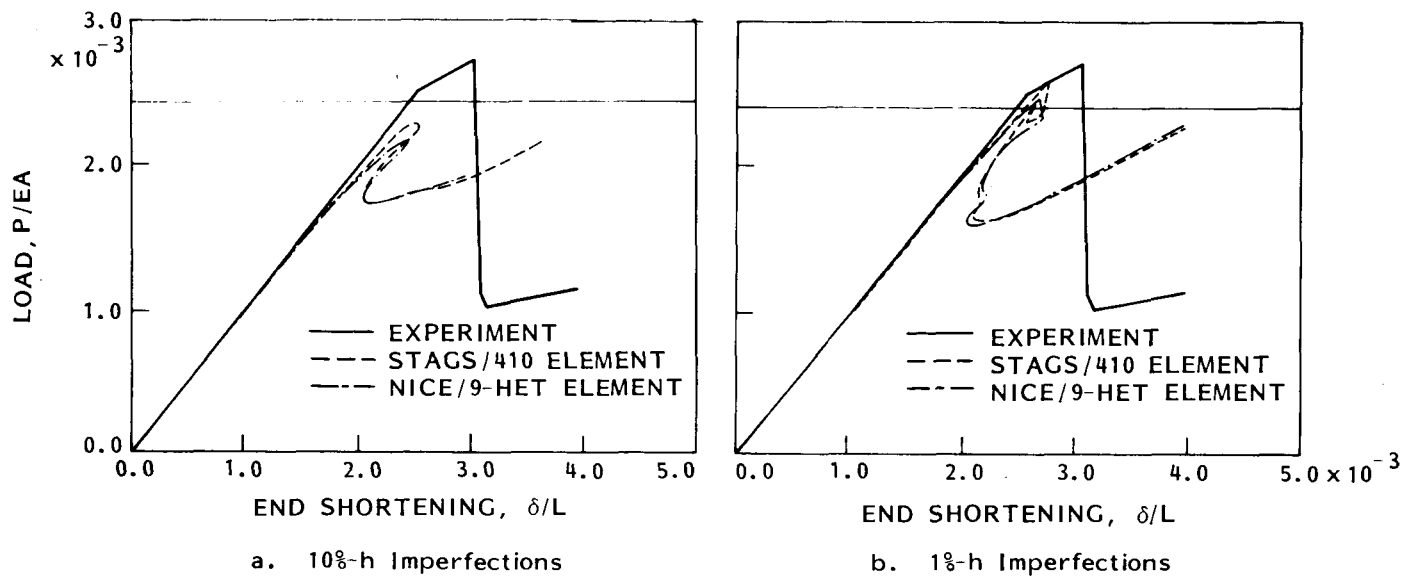


Figure 11. Corroboration with the STAGS code, postbuckling analyses.

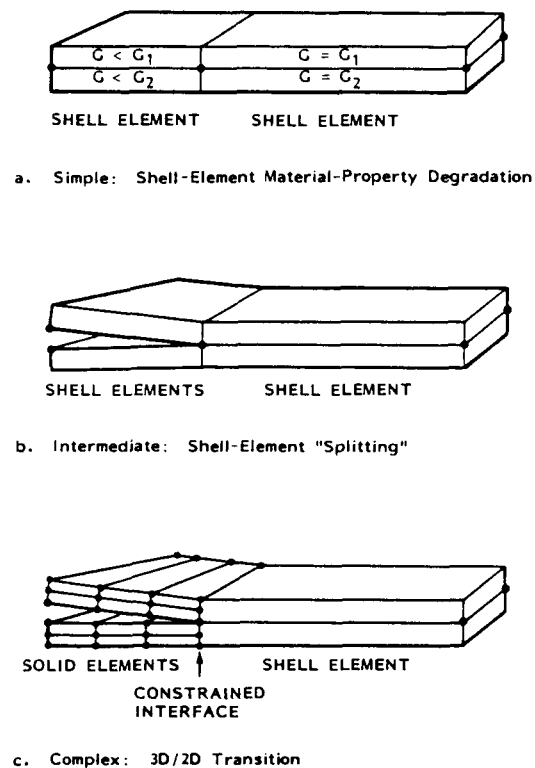


Figure 12. Composite failure-progression models.